Thermal buckling and symmetry breaking in thin ribbons under compression

Paul Z. Hanakata^{a,*}, Sourav S. Bhabesh^{b,1}, Mark J. Bowick^c, David R. Nelson^d, David Yllanes^{e,f,c}

^a Department of Physics, Harvard University, Cambridge, MA 02138, USA
 ^b Amazon Web Services (AWS), Washington DC Metro Area, USA
 ^c Kavli Institute for Theoretical Physics, University of California, Santa Barbara, CA 93106, USA
 ^d Department of Physics, Lyman Laboratory of Physics and School of Engineering and Applied Sciences, Harvard University, Cambridge, MA 02138, USA

 $^eChan\ Zuckerberg\ Biohub,\ San\ Francisco,\ CA\ 94158,\ USA$ $^fInstituto\ de\ Biocomputación\ y\ Física\ de\ Sistemas\ Complejos\ (BIFI),\ 50009\ Zaragoza,\ Spain$

Abstract

Understanding thin sheets, ranging from the macro to the nanoscale, can allow control of mechanical properties such as deformability. Out-of-plane buckling due to in-plane compression can be a key feature in designing new materials. While thin-plate theory can predict critical buckling thresholds for thin frames and nanoribbons at very low temperatures, a unifying framework to describe the effects of thermal fluctuations on buckling at more elevated temperatures presents subtle difficulties. We develop and test a theoretical approach that includes both an in-plane compression and an out-of-plane perturbing field to describe the mechanics of thermalised ribbons above and below the buckling transition. We show that, once the elastic constants are renormalised to take into account the ribbon's width (in units of the thermal length scale), we can map the physics onto a mean-field treatment of buckling, provided the length is short compared to a ribbon persistence length. Our theoretical predictions are checked by extensive molecular dynamics simulations of thin thermalised ribbons under axial compression.

Keywords:

1. Introduction

Thin sheets, possibly with embedded kirigami cuts, have been the object of intense recent study [1]. A careful design allows membranes with cuts to stretch far beyond their pristine limits [2–7], to have non-linear post-buckling behaviours [8, 9], and even to exhibit complex motions such as roll, pitch, yaw, and lift [10]. Many of these novel effects arise due to out-of-plane deflections, i.e., escape into the third dimension. With such mechanical versatility and straightforward actuation, kirigami sheets have been used as building blocks for soft robots, flexible biosensors and artificial muscles [11, 12]. A full theoretical framework for this rich phenomenology must rest on a thorough understanding of the fundamental mechanical effects. In particular, out-of-plane motion in simple kirigami systems (e.g., a sheet with a single slit) have been described as an Euler buckling problem [10]. The buckling of pillars and plates has been studied for centuries, but a unifying theory to understand buckling in nanosystems when thermal fluctuations become important, as in the case of molecularly thin materials such as MoS₂ and graphene [13], is still lacking.

In the classical description, the dimensionless Föpplvon Kármán number vK = YW_0L_0/κ , where Y is the 2D Young's modulus, κ is the bending rigidity, W_0 and L_0 are respectively the T=0 width and length of the ribbon, can be used to quantify the ease of buckling a thin sheet out of plane at zero temperature. The picture is more complicated for thermalised membranes [14], where Y and κ become scale dependent and, in particular, the bending rigidity is dramatically enhanced [15–20]. This longstanding theoretical prediction is consistent with an important study of graphene ribbons by Blees et al. [2]. Using a cantilever setup, the effective bending rigidity of micron-size graphene at room temperature was found to increase by a factor of roughly 4000 relative to the zerotemperature microscopic value. Although it is possible that some of this increase may be due to quenched random disorder in the graphene ribbons [21], these room temperature experiments nevertheless demonstrate a striking enhancement over the T=0 density functional theory predictions [22]. When thermal fluctuations are important, classical Euler buckling predictions break down. In fact, in such an entropy-dominated high-temperature setting, some aspects of nanoribbon behaviours have more in common with linear polymers with long persistence length [23].

In this letter, we investigate (i) to what temperature classical Euler buckling still holds, (ii) how we can locate buckling transitions in fluctuating ribbons under compression, and (iii) how these buckling transitions change with temperature and with the ribbon dimensions. To

 $^{^*}$ Corresponding author.

Email address: paul.hanakata@gmail.com (Paul Z. Hanakata)

¹Work completed prior to joining AWS.

this end, we develop a mean-field theory (MFT) approach to the buckling of thermalised ribbon under longitudinal compression and use molecular dynamics simulations to check our predictions. The applicability of our MFT is determined by two crucial length scales: First, the thermal length $\ell_{\rm th} \sim \kappa/\sqrt{Yk_{\rm B}T}$, where $k_{\rm B}$ is the Boltzmann constant, T is the temperature, Y and κ are the microscopic 2D Young's modulus and bending rigidity respectively. And second, the one-dimensional persistence length $\ell_{\rm p} = 2\kappa W_0/k_{\rm B}T$. We are interested in the regime $\ell_{\rm th} < W_0 < L_0 < \ell_{\rm p}$, where the temperature is high enough that $\ell_{\rm th}$ is smaller than the ribbon's width W_0 , so thermal renormalisation is significant, but not so high that $\ell_{\rm p}$ becomes small compared to the ribbon length L_0 .

Our theory predicts, and our simulations confirm, that the buckling transition is delayed, because the renormalised $Y_{\rm R}$ becomes softer and the renormalised $\kappa_{\rm R}$ becomes stiffer as T increases. We also explore the possibility of utilising an out-of-plane uniform perturbation (e.g., an electric or gravitational field) to break the height-reversal symmetry. Such fields give an alternative path to control the buckling transition. Overall, our study provides a new framework to study buckling in thermalised ribbons which is relevant to nanomaterials, such as graphene or MoS₂, or to biological systems when the thermal scale is comparable to or less than the system size. While this work was in progress, we learned of interesting work by Morshedifard et al. [24], who carried out simulations similar to ours, without, however the introduction of a symmetry-breaking field, and without the post-buckling mean-field theory used here.

2. Model and methods

2.1. Coarse-grained model

We consider a rectangular sheet of size $L_0 \times W_0$, with $L_0 > W_0$, which is discretised by a triangular lattice of unbreakable bonds, in the crystalline membrane paradigm [26] The triangular lattice used here can be considered as a convenient dual representation to the honeycomb lattice usually employed to model graphene. We use the notation L_0 to distinguish the T=0 rest length from the projected length after thermal shrinking or compression. Neighbouring nodes are connected by harmonic springs and there is an energy cost when the normals (n_α) of neighbouring plaquettes are not aligned. The total energy is given by

$$\mathcal{H} = \frac{k}{2} \sum_{\langle i,j \rangle} (|\boldsymbol{r}_i - \boldsymbol{r}_j| - a)^2 + \hat{\kappa} \sum_{\langle \alpha,\beta \rangle} (1 - \boldsymbol{n}_\alpha \cdot \boldsymbol{n}_\beta)$$
 (1)

where k is the harmonic spring constant, $\hat{\kappa}$ is the microscopic bending rigidity and a is the preferred length between two neighbouring nodes which also sets our unit of length. The first sum is over neighbouring nodes and the second over neighbouring triangular plaquettes. A schematic is shown in Fig. 1(a). Our discretised bare elastic constants are related to the bare continuum ones by $\kappa = \sqrt{3}\hat{\kappa}/2$ and $Y = 2k/\sqrt{3}$ [27].

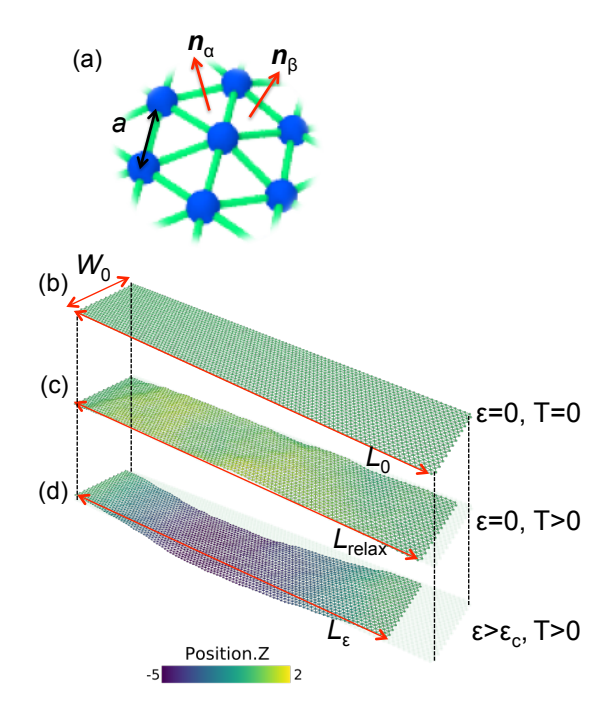


Figure 1: (a) Schematic of nodes on a triangular lattice. (b) Ribbon in its flat rest configuration at T=0, with length L_0 and width W_0 . (c) Relaxed ribbon at T>0 and zero compression. The thermal ripples cause the ribbon to shrink from its rest length L_0 down to a thermal projected length $L_{\rm relax}$. (d) Ribbon at a non-zero temperature and compressed beyond the critical buckling strain $\epsilon_{\rm c}$. In panels (b)–(d) each end of a ribbon is clamped to have width W_0 and the colour map shows the height of each node relative to z=0 at the two ends. We used OVITO software to visualise the ribbons [25].

2.2. Parameters and length scales

Since we are interested in relatively narrow ribbons, we use $L_0 \sim 100a$ and $W_0 \sim 20a$ (2500 nodes). Following previous work [28–30], we set $k = 1440\hat{\kappa}/a^2$, which gives us a Föppl-von Kármán number of vK $\sim 10^6$, comparable to micron-size 2D materials such as graphene and MoS₂.

As we change the temperature, keeping $k/\hat{\kappa}$ fixed, two crucial length scales, the thermal and persistence lengths, will vary [23, 29]:

$$\ell_{\rm th} = \sqrt{\frac{\pi^3 64\kappa^2}{3k_{\rm B}TY}},\tag{2}$$

$$\ell_{\rm p} = \frac{2\kappa W_0}{k_{\rm B}T}.\tag{3}$$

We want here to adapt the zero-temperature theory to temperatures high enough for thermal renormalisation to become significant. The temperature should not, however, be so high that $\ell_{\rm p}$ becomes small compared to L_0 (i.e., we stay far away from the ribbon crumpling regime). In simulations we fixed L_0, W_0 and $k/\hat{\kappa}$ while varying $\hat{\kappa}$ and T. We simulated over a temperature range $10^{-7} \leq k_{\rm B}T/\hat{\kappa} \leq 4$ or equivalently $10^{-2} \lesssim W_0/\ell_{\rm th} \lesssim 10^2$. In the following we shall use $W_0/\ell_{\rm th}$ as the natural variable for the tempera-

ture scaling of the system, and focus on the regime where $W_0 > \ell_{\rm th}$.

2.3. Clamped boundary conditions and molecular dynamics simulations

We use the HOOMD package [31] to simulate model (1) in the NVT ensemble with a Nosé-Hoover thermostat. In order to study the buckling dynamics, we clamp the ribbon by fixing the nodes on the first two rows at both ends. We vary the distance between the clamped edges to induce the desired strain. Importantly, we thus operate in a constant-strain ensemble.

Because of thermal fluctuations, the ribbon shrinks from from its T=0 rest length L_0 . We define $L_{\rm relax}$ as the projected natural length at which all stress components are zero and define the incremental compressive strain as $\epsilon=1-L_\epsilon/L_{\rm relax}$, where L_ϵ is the projected length at a given compressive strain ϵ . At finite T we have therefore the inequalities $L_{\epsilon>0} < L_{\rm relax} < L_0$, illustrated in Fig. 1.

Following [29], we use a timestep of $\Delta t = 0.0025\tau$ where τ is the Lennard-Jones time $\tau = \sqrt{ma^2/k_{\rm B}T}$ and we use natural units of mass and energy m=a=1. Our clamped systems are simulated in the NVT ensemble for 10^7 steps, saving a snapshot every 10^4 steps. For each choice of parameters, we simulate either 5 or (more commonly) 10 independent runs. We use a jackknife method (see, e.g., [32]) to estimate statistical errors.

3. Theoretical expectations

The most dramatic signature of the buckling transition occurs in stress-strain curves. Fig. 2 shows the stress as a function of the strain as measured from our simulations when T=0, then at a low T such that $W_0/\ell_{\rm th}=0.3$, and finally at a more elevated temperature such that $W_0/\ell_{\rm th}=8.5$, where thermal fluctuations have a stronger effect. The computed Young's modulus, critical stress, and critical strain for T=0 are within 10% of the theoretical predictions $[\frac{Y^{\rm simulation}}{Y^{\rm theory}}=0.99, \frac{\sigma_{\rm cheory}^{\rm simulation}}{\sigma_{\rm cheory}^{\rm theory}}=0.92, \frac{\epsilon_{\rm cheory}^{\rm simulation}}{\epsilon_{\rm c}^{\rm theory}}=0.94]$. We attribute the small deviations to our discretised clamped boundary conditions. The stress-strain curves can be understood via the following simple argument: we write the energy of a possibly bent compressed ribbon of width W_0 , with displacements uniform along the y direction, as

$$E/W_0 = \frac{1}{2}Y \int_{-L/2}^{L/2} \left(\frac{\mathrm{d}u(x)}{\mathrm{d}x}\right)^2 \mathrm{d}x - \sigma_{xx}d + \frac{1}{2}\kappa \int_{-L/2}^{L/2} \left(\frac{\mathrm{d}^2h(x)}{\mathrm{d}x^2}\right)^2, \tag{4}$$

where u(x) is the displacement field along the x axis, h(x) the displacement perpendicular to the ribbon, and $-\sigma_{xx}d$ represents the work done by a force $F = W_0\sigma_{xx}$ to compress the ribbon an amount d along \hat{x} relative to its natural length L. Here, Y and κ are the 2D Young's modulus

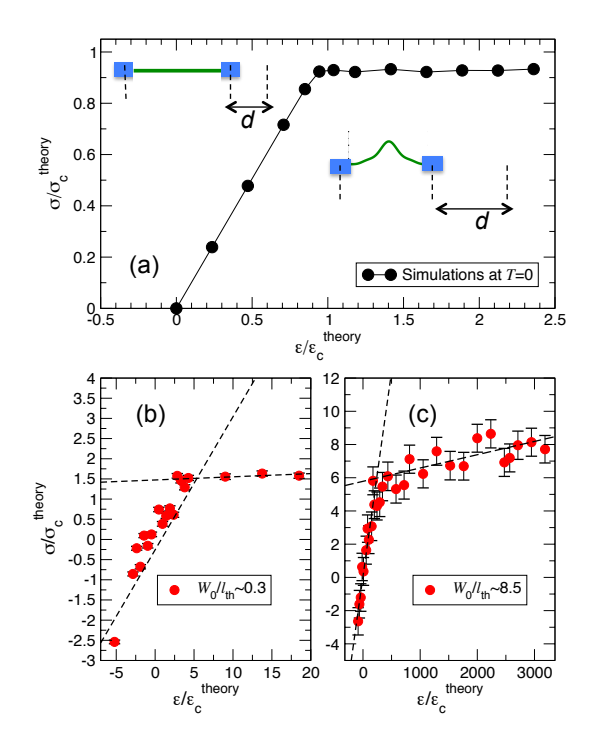


Figure 2: (a) Stress as a function of compressive strain scaled by their zero-temperature critical values ($\sigma_{\rm c}^{\rm theory}$ and $\epsilon_{\rm c}^{\rm theory}$) for a ribbon at (a) T=0, (b) $W_0/\ell_{\rm th}=0.3$ and (c) $W_0/\ell_{\rm th}=0.3$. The dotted lines are linear fits in the pre-buckling (small- ϵ) regime and in the post-buckling regime $\epsilon > \epsilon_{\rm c}$. The scaled critical stress, which is proportional to the renormalised bending rigidity $\kappa_{\rm R}$, increases with increasing $W_0/\ell_{\rm th}$ (or temperature). In contrast, the slope (Y_R) becomes smaller with increasing $W_0/\ell_{\rm th}$. Note that the very different horizontal scales in (b) and (c).

and bending rigidity which measure the compressional and bending energies respectively. In the compressed, but unbuckled, state the strain is $\epsilon = \frac{\mathrm{d}u(x)}{\mathrm{d}x} = d/L$ and from Eq. (4), the compressional energy is $E_{\mathrm{comp}} = \frac{1}{2}W_0Yd^2/L$. In this regime, we minimise over d to find Hooke's Law $\sigma = F/W_0 = Y\epsilon$, which accounts for the first, linear part of the stress-strain curve. Beyond the critical strain ϵ_c , however, the system prefers to trade compressional energy for bending energy. As we shall discuss below, for tangential boundary conditions at two ribbon ends, as is the case for our simulations, we have the usual buckling instability when $\epsilon > \epsilon_c$, $\epsilon_c = 4\pi^2\kappa/(YL^2)$ [33].

What is the incremental stress $\delta\sigma$ associated with an additional strain $\delta\epsilon = \delta d/L$ when $\epsilon > \epsilon_{\rm c}$? To this end, we assume the compressional energy vanishes. We can now regard x as a coordinate embedded in the ribbon. Note that the tipping angle $\theta(x)$ of the normal away from the z-axis is given by $\theta(x) \approx \frac{dh}{dx}$, so that the additional energy associated with the buckled state can be rewritten as

$$\Delta E/W_0 \approx \frac{1}{2}\kappa \int_{-L/2}^{L/2} \left(\frac{\mathrm{d}\theta(x)}{\mathrm{d}x}\right)^2 \mathrm{d}x - \delta\sigma d,$$
 (5)

where $-\delta\sigma W_0 d$ is the extra work done beyond the buckling transition by the stress increment $\delta\sigma$. Once buckling leads to a ribbon with a well-developed looping arch, i.e., $\epsilon\gg\epsilon_{\rm c}$ we expect that $\frac{{\rm d}\theta(x)}{{\rm d}x}\sim\frac{\pi d}{L^2}$ so that the normal turns an angle $\delta\theta\sim\pi/2$ when $d\sim L/2$. The energy associated with Eq. (5) is then $\Delta E\sim W_0\kappa d^2/L^3$. Upon minimising this expression over d, we obtain

$$\delta \sigma_{xx} = \text{const.} \frac{\kappa d}{L^3} \approx \text{const.} \frac{\kappa}{L^2} \delta \epsilon.$$
 (6)

Thus, the slope of the stress-strain curve beyond $\epsilon_{\rm c}$, once the buckling transition becomes well developed, should be of the order κ/L^2 , as might have been guessed from dimensional analysis.

We conclude that the ratio of the pre- and post-buckling slopes is $\sim YL^2/\kappa$, i.e., it is of the order the Föppl-von Kármán number $\sim 10^6$ in our simulations! Hence, it is not surprising that the zero-temperature stress-strain curve looks nearly flat in Fig. 2(a).² There is, however, a hint of a non-zero slope at finite temperatures in our simulations when $W_0/\ell_{\rm th} = 0.3$, which becomes more pronounced when $W_0/\ell_{\rm th}=8.5$. As discussed below, we attribute this enhanced post-buckling slope to a strong W_0 -dependent upward renormalization bending rigidity $\kappa \to \kappa_{\rm R}$, due to thermal fluctuations. Moreover, by rescaling the stress and the strain with their respective zero-temperature critical buckling compression and strain, we can see that the critical strain and critical buckling compression increase with increasing T, or equivalently increasing $W_0/\ell_{\rm th}$, as shown in Fig. 2(b) and (c).

The argument above cannot tell us the details of what happens close to ϵ_c , where one must account for delicate balance between compression and bending energies. To understand this regime, we now construct a simple Landau-like theory of the buckling transition, appropriate to the constant-strain ensemble enforced by our constant NVT simulations.

3.1. Mean-field theory

As the ribbon is compressed along the longitudinal x direction it can both compress and deflect out of plane in the z direction. We work in the Monge representation and denote the vertical displacement by h(x,y). In this derivation we denote the instantaneous projected length after a compression d (to produce a dimensionless compressive strain ϵ) by L_{ϵ} . To control the buckling order parameter, we also impose an out-of-plane electric field \mathcal{E} coupled to the height of a charged ribbon, generating a potential energy $V_{\perp} = -\int_{-L_{\epsilon}/2}^{L_{\epsilon}/2} \rho \mathcal{E} \ h(\vec{x}) \ d^{2}x$, where $\rho = Q/(L_{0}W_{0})$ is the charge density. To describe a ribbon in a gravitational field we simply need to substitute $\rho = m/(L_{0}W_{0})$ and $\mathcal{E} = g$. We assume a large Föppl-von Kármán number $YL_{0}W_{0}/\kappa$ (easily achieved for graphene and MoS₂),

in which the stretching along the ribbon will be comparatively small. The total free-energy cost is given by

$$G = \frac{1}{2} \int d^2x \left[\left(\nabla^2 h \right)^2 + 2\mu u_{ij}^2 + \lambda u_{kk}^2 \right] - \rho \mathcal{E} \int d^2x h$$
$$-\sigma \int d^2x (\partial_x u_x), \tag{7}$$

where $u_{ij} = (\partial_i u_j + \partial_j u_i)/2 + (\partial_i h)(\partial_j h)/2$ and $\sigma_{xx} = \sigma$ denotes a uniaxial stress at the clamped edges. Notice that, since the centre-of-mass height is $h_{\mathrm{C}M} = \frac{1}{W_0 L_0} \int \mathrm{d}^2 x h(\vec{x})$, we can write $G = G_0 - \mathcal{E}Qh_{\mathrm{CM}}$ and the thermally averaged centre-of-mass height h_{CM} in the full fluctuating which we are only approximating here

$$\langle h_{\rm CM} \rangle = \frac{1}{Z} \int \mathcal{D}[h, u_i] h_{\rm CM} e^{-(G_0 - \mathcal{E}Qh_{\rm CM})/k_{\rm B}T},$$
 (8)

where $Z = \int \mathcal{D}[h, u_i] e^{-E/k_B T}$ is the partition function. Since we are interested in the buckling response due to an external field, we also study the height susceptibility defined as $\chi = d\langle h_{CM} \rangle/d\mathcal{E}$. Upon using Eq. (8) we obtain

$$\chi \propto \langle h_{\rm CM}^2 \rangle - \langle h_{\rm CM} \rangle^2.$$
 (9)

We can further simply the physics into a 1D buckling problem. We approximate $h(x,y)\approx h(x)$ and define charge density $\rho=Q/L_0$, an effective 1D bending rigidity and Young's modulus given by $\kappa_{\rm 1D}=\kappa W_0$ and $Y_{\rm 1D}=YW_0$, respectively, where κ and Y denote T=0 values of the elastic constants. Within a Monge representation, we can approximate $L_\epsilon+d\simeq L_\epsilon+\frac{1}{2}\int_{-L_\epsilon/2}^{L_\epsilon/2}\left(\frac{{\rm d}h}{{\rm d}x}\right)^2{\rm d}x$, where the strain ϵ is given by $\epsilon=d/L_{\rm relax}$. The total energy then consists of bending, stretching and work done by the external compressive force F and an out-of-plane field,

$$G[h, \mathcal{E}] = \frac{\kappa_{1D}}{2} \int_{-L_{\epsilon}/2}^{L_{\epsilon}/2} dx \left(\frac{d^{2}h}{dx^{2}}\right)^{2} + \frac{Y_{1D}}{2L_{\epsilon}} \left[\int_{-L_{\epsilon}/2}^{L_{\epsilon}/2} dx \frac{1}{2} \left(\frac{dh}{dx}\right)^{2}\right]^{2}$$

$$-\frac{F}{2} \int_{-L_{\epsilon}/2}^{L_{\epsilon}/2} dx \left(\frac{dh}{dx}\right)^{2} - \rho \mathcal{E} \int_{-L_{\epsilon}/2}^{L_{\epsilon}/2} h dx.$$
(10)

Note that we have eliminated, or "integrated out", the in-plane phonons. See Appendix C for a detailed derivation of Eq. (10), which incorporates our constant-strain boundary conditions. Note also the non-local character of the second, stretching term. Lifshitz and Cross [34] have described equations of motion for micro-electromechanical devices with a similar non-local term. The ansatz of the first buckling mode $h(x) = \frac{1}{2}h_{\rm M}\left[1+\cos\left(\frac{2\pi x}{L_\epsilon}\right)\right]$, which allows for a height $h_{\rm M}$ midway between the clamps and satisfies the boundary conditions $\frac{{\rm d}h}{{\rm d}x}\big|_{x=\pm L_\epsilon/2}=0$, then

²Both the critical strain $\epsilon_{\rm c} \sim \kappa/(YL^2)$ and the post-buckling slope $\sim \kappa/L_0^2$ vanish in the thermodynamic limit $L_0 \to \infty$.

leads to an expansion in the buckling amplitude $h_{
m M}$

$$G = \frac{\pi^2}{4L_{\epsilon}} \left(\frac{4\kappa_{1D}\pi^2}{L_{\epsilon}^2} - F \right) h_{\rm M}^2 + \frac{\pi^4 Y_{1D}}{32L_{\epsilon}^3} h_{\rm M}^4 - \frac{\rho L_{\epsilon}\mathcal{E}}{2} h_{\rm M}. \tag{11}$$

Note that, although Eq. (11) resembles a Landau theory near a critical point, the expansion parameter depends in a non-trivial way on the system dimension L_{ϵ} . Note also that the single mode approximation only makes sense close to the transition; many more Fourier modes would be required to describe the fully developed post-buckling looping arch that develops for large strains, as in Fig. 2(a).

3.2. Euler buckling at T=0

For $\mathcal{E}=0$, we can minimise Eq. (11) over $h_{\rm M}$ to obtain a critical 2D compressive stress of $\sigma_{\rm c}=4\pi^2\kappa/L_{\epsilon_{\rm c}}^2$, and a corresponding critical buckling strain $\epsilon_{\rm c}=\sigma_{\rm c}/Y=\frac{4\pi^2\kappa}{YL_{\epsilon_{\rm c}}^2}$, where $L_{\epsilon_{\rm c}}$ is the projected length at the critical buckling strain.³ These are the critical load and critical strain of classical Euler buckling with tangential boundary conditions [33]. The buckling amplitude is then

$$h_{\rm M} = \begin{cases} 0, & \epsilon < \epsilon_{\rm c} \text{ (or } \sigma < \sigma_{\rm c}), \\ \pm \frac{2L_{\epsilon_{\rm c}}}{\pi} \sqrt{\epsilon - \frac{4\kappa\pi^2}{YL_{\epsilon_{\rm c}}^2}}, & \epsilon \ge \epsilon_{\rm c} \text{ (or } \sigma \ge \sigma_{\rm c}). \end{cases}$$
(12)

To test the above approach, we compared simulations at T=0 with the analytical predictions. These simulations reproduced the square-root scaling predicted by the theory and yielded consistent values for the Young's modulus, critical stress and critical strain (see Appendix A for details and plots).

3.3. Response function near critical buckling

At the critical point the system becomes sensitive to external perturbation. In analogy with the magnetic susceptibility of an Ising system, within the MFT we can define a height susceptibility as the linear response to a uniform out-of-plane external field,

$$\chi \equiv \frac{\partial h_{\rm M}}{\partial \mathcal{E}} \bigg|_{\mathcal{E}=0} = \begin{cases} \frac{Q}{Y\pi^2} \frac{L_{\epsilon_{\rm c}}}{W_0} (\epsilon_{\rm c} - \epsilon)^{-1} & \text{if } \epsilon < \epsilon_{\rm c} \\ \frac{Q}{2Y\pi^2} \frac{L_{\epsilon_{\rm c}}}{W_0} (\epsilon - \epsilon_{\rm c})^{-1} & \text{if } \epsilon > \epsilon_{\rm c}. \end{cases}$$
(13)

This response function diverges at the buckling transition. Hence, the system becomes infinitely sensitive to the out-of-plane field $\mathcal E$ as the buckling transition is approached. Note also that χ is larger for small aspect ratio W_0/L_ϵ . Eq. (11) predicts a non-linear dependence of the buckling amplitude $h_{\rm M}$ on $\mathcal E$ when $\epsilon=\epsilon_{\rm c}$

$$h_{\rm M} = L_{\epsilon_{\rm c}} \left(\frac{4Q\mathcal{E}}{\pi^4 Y W_0} \right)^{1/3} . \tag{14}$$

The finite-temperature generalisation of this susceptibility is given by Eq. (9).

3.4. Thermalised Euler buckling

As the temperature increases and the thermal length $\ell_{\rm th}({\rm see~Eq.}~(2))$ becomes smaller than the membrane's dimensions, the elastic constants of the system are renormalised. For ribbons with $W_0 < L_0$ this renormalisation is cut off by the width and leads to the following renormalized elastic constants [23]:

$$\kappa_{\rm R}(W) \simeq \begin{cases} \kappa & \text{if } W_0 < \ell_{\rm th}, \\ \kappa \left(\frac{W_0}{\ell_{\rm th}}\right)^{\eta} & \text{if } W_0 > \ell_{\rm th}, \end{cases}$$
(15)

$$Y_{\rm R}(W) \simeq \begin{cases} Y & \text{if } W_0 < \ell_{\rm th} \\ Y\left(\frac{W_0}{\ell_{\rm th}}\right)^{-\eta_u} & \text{if } W_0 > \ell_{\rm th}, \end{cases}$$
(16)

where $\eta \approx 0.8-0.85$ and $\eta_u \approx 0.3-0.4$ from analytical computations [18, 23, 35] and molecular dynamics or Monte Carlo simulations [20, 28, 36, 37]. We expect, therefore, a strongly W_0 and temperature-dependent stiffening in the bending rigidity and softening in the Young's modulus. Upon substituting the renormalised elastic constants in to the MFT, we obtain a scaling for the critical 2D stress of $\sigma_c \propto (W_0/\ell_{\rm th})^\eta$ and a critical buckling strain $\epsilon_{\rm c} \propto (W_0/\ell_{\rm th})^{\eta+\eta_u}$. Because $\ell_{\rm th} \propto T^{-1/2}$ and using $\eta \approx 0.8$ and the scaling relation [16] $2\eta + \eta_u = 2$, we see that σ_c and ϵ_c are predicted to increase with increasing temperature with non-trivial power laws, $\epsilon_c \sim T^{0.6}$ and $\sigma_c \sim T^{0.4}$.

4. Numerical results for finite temperature

The MFT section explains how we can use the maximum height $h_{\rm M}$ of a compressed ribbon as an order parameter for a buckling transition and estimate how the critical strain and critical stress will shift with increasing temperature. We now test this theoretical prediction against molecular dynamics simulations. We use the notation $\langle O \rangle$ for the average in the NVT ensemble of the observable O.

It will be convenient to replace $h_{\rm M}$ by the height of the ribbon centre of mass $h_{\rm CM}=\frac{1}{N}\sum_i h_i$ as our order parameter. There is, however, a subtle point to be considered. In the absence of an external field ($\mathcal{E}=0$) our energy (10) is invariant with respect to height-inversion symmetry. This means that configurations with $h_{\rm CM}=\pm h$ have the same probability and would seem incompatible with the result $\langle h_{\rm CM} \rangle \neq 0$ for $\epsilon > \epsilon_{\rm c}$. As with conventional magnetic phase transitions, this apparent paradox is resolved by realising that, in the limit of large system sizes, the system undergoes spontaneous symmetry breaking [38]. Formally, we could consider a small symmetry-breaking field \mathcal{E} to establish a preferred direction and take the double limit

$$\langle h_{\rm CM} \rangle = \lim_{\mathcal{E} \to 0} \lim_{A \to \infty} \langle h_{\rm CM} \rangle_A,$$
 (17)

where A denotes the system size. Notice that if we reversed the order of the limits $\langle h_{\rm CM} \rangle$ would always vanish. This is the situation in any computer simulation, where flips

 $^{^3 \}mathrm{For}$ a very large Föppl-von Kármán number vK we can approximate L_ϵ as L_0

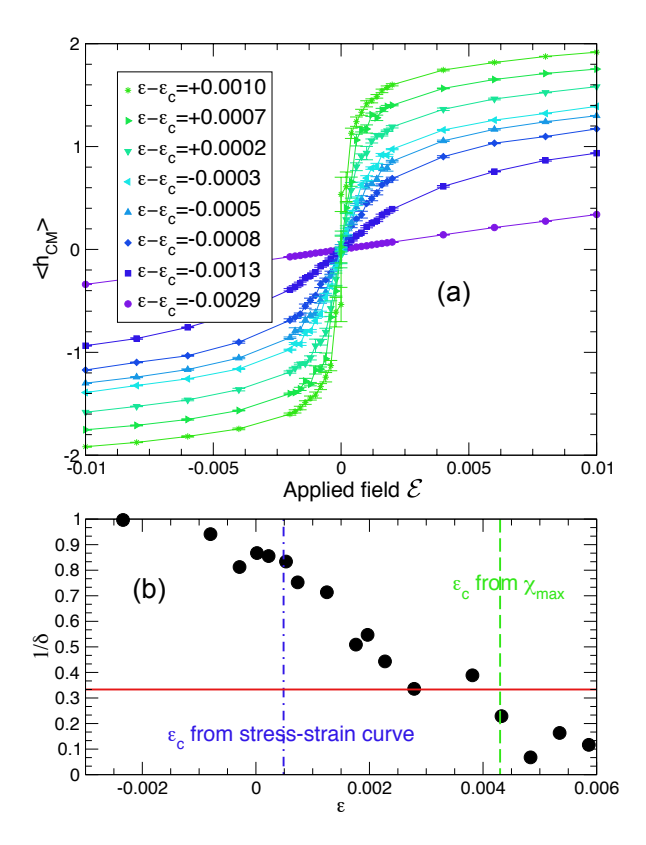


Figure 3: (a) The height centre of mass $\langle h_{\rm CM} \rangle$ as a function of the out-of-plane field $\mathcal E$ for different strains relative to critical strain $\epsilon_{\rm c}$ obtained from the stress-strain curve. The slope (susceptibility) increases closer to the buckling transition. (b) The exponent $1/\delta$ as a function of ϵ . The critical strain obtained from the height susceptibility χ (green vertical dashed line) does not coincide with the $\epsilon_{\rm c}$ obtained from the stress-strain curve (blue vertical dashed line). We see that $h_{\rm CM} \propto \mathcal E$ far below the buckling transition and that it becomes more sensitive (smaller $1/\delta$) as the system becomes closer to the transition. The $1/\delta$ exponent is close to 1/3 (red horizontal line) when ϵ is close to the value when χ is at maximum.

between the up and down states are always possible after a finite long time. The metastable dynamics for $\mathcal{E} = 0$ and the behaviour of the flipping time for a molecular dynamics simulation will be considered in a future work [39].

The previous discussion is in complete analogy to the magnetisation m of a magnetic system, where m plays the role of our height variable. In Appendix B we explore the behaviour of the susceptibility $\chi = \frac{\mathrm{d} h_{\mathrm{CM}}}{\mathrm{d} \mathcal{E}}\big|_{\mathcal{E}=0}$ via simulations and find that these fluctuations become very large as the buckling transition is approached from below.

4.1. Buckling induced by an external field

The definition of the broken-symmetry phase becomes difficult for finite sizes, since the ribbon can always flip between the up and down states. We can break this degeneracy by applying an external field perpendicular to the plane. From Eq. (14) we expect steep curves of $\langle h_{\rm CM} \rangle_{\mathcal{E}}$

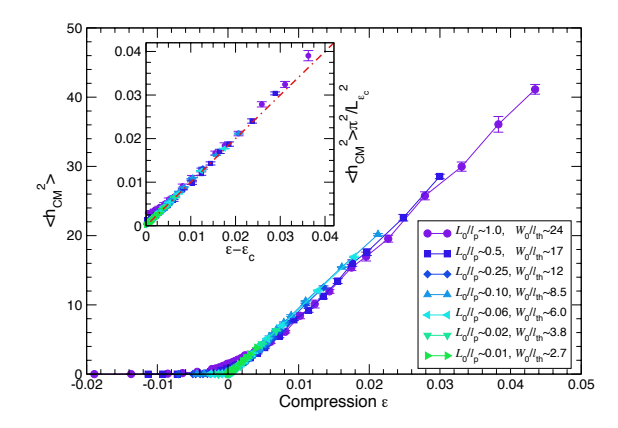


Figure 4: Average of the squared centre-of-mass height $\langle h_{\rm CM}^2 \rangle$ as a function of compressive strain ϵ when $\mathcal{E}=0$. In the pre-buckling region $\langle h_{\rm CM}^2 \rangle$ is close to zero, whereas in the post-buckling region $\langle h_{\rm CM}^2 \rangle$ goes linearly with ϵ . The inset shows the dimensionless order parameter $\langle h_{\rm CM}^2 \rangle \pi^2 / L_{\epsilon_c}^2$ as a function of $\epsilon - \epsilon_c$. The collapse of all data with a slope of one, as in Eq. (19), agrees with our mean-field theory.

as $\mathcal{E} \to 0$, near the buckling transition, or equivalently $\frac{dh_{\rm CM}}{d\mathcal{E}} \propto \mathcal{E}^{-2/3}$.

We can test this prediction in MD simulations by changing the perturbing field for compressions at a constant temperature. Specifically, we simulate ribbons with $W_0/\ell_{\rm th} \sim$ $8.5 (k_{\rm B}T/\hat{\kappa}=0.05)$ and apply an \mathcal{E} up to 0.01. To save computing time we only simulated $\mathcal{E} > 0$. In Fig. 3(a), we see that well below the buckling transition the average centre-of-mass height $\langle h_{\rm CM} \rangle$ is weakly dependent on the field. As we approach the critical buckling strain, $\frac{dh_{\rm CM}}{d\mathcal{E}}\Big|_{\mathcal{E}=0}$ becomes larger. Along the iso-strain $\epsilon=\epsilon_{\rm c}$ where χ is at maximum, we expect $\langle h_{\rm CM} \rangle \propto \mathcal{E}^{1/\delta}$ where $\delta = 3$ (see Eq. 14). We can fit our data to calculate exponent δ . In Fig. 3(b) we also plot the critical strain obtained from stress-strain curve and from the peak of the height susceptibility χ . Interestingly, we find a proportionality between the critical strains obtained from stressstrain curves and critical strains obtained from the peaks of χ ; however, these two values do not coincide exactly (see Appendix C for more details). We find that $1/\delta$ is close to 1/3 as ϵ approaches ϵ_c , where χ is maximum. We hope to investigate this proportionality in future work. Similar to magnetic-based memories, one could use the up and down buckling in a double-clamped ribbon to store information, which can be controlled by compression ϵ , temperature T, or perturbing out-of-plane field \mathcal{E} .

4.2. The centre-of-mass height behaviour under compression

As we discussed earlier we can locate the buckling transitions from stress-strain curves using data like those in Fig. 2. We expect these curves will have a constant slope

close to $\epsilon=0$, given by the Young's modulus, and another slope $\sim \kappa_{\rm R}/L_{\epsilon}^2$ beyond the buckling point. The crossing point of the pre- and post-buckling curves gives the critical buckling load $\sigma_{\rm c}$ and critical strain $\epsilon_{\rm c}$ (see Appendix B for more details).

To provide a more quantitative test of the MFT, we can use the relation $h_{\text{CM}}^2 = \left(\frac{1}{L_{\epsilon}} \int_{-L_{\epsilon}/2}^{L_{\epsilon}/2} h \, \mathrm{d}x\right)^2 = \frac{1}{4} h_{\text{M}}^2$ to define a dimensionless buckling parameter at T=0:

$$\frac{h_{\rm CM}^2 \pi^2}{L_{\epsilon_c}^2 (T=0)} = \epsilon - \epsilon_{\rm c}(T=0), \tag{18}$$

where $\epsilon_{\rm c}(T=0) = \frac{4\kappa\pi^2}{YL_{\epsilon_{\rm c}}^2(T=0)}$. At finite temperature, we expect the same relation to hold, with the corresponding $\epsilon_{\rm c}$ given by the renormalised constants:

$$\frac{\langle h_{\rm CM}^2 \rangle \pi^2}{L_{\epsilon_{\rm c}}^2} = \epsilon - \epsilon_{\rm c}. \tag{19}$$

Note that, at finite T, L_{ϵ_c} and $L_{\rm relax}$ are temperature dependent. Fig. 4 shows $\langle h_{\rm CM}^2 \rangle$ as a function of ϵ for different $W_0/\ell_{\rm th}$. The linear dependence is clear. To test the MFT prediction, we subtract $\epsilon_{\rm c}$, found previously from the stress-strain curve analyses, from ϵ . Remarkably, we indeed find a data collapse with a slope of one for $\epsilon > \epsilon_{\rm c}$, in accordance with MFT and Eq. (19). At high temperatures, however, the transitions grow less sharp, presumably due to finite-size effects.

4.3. The renormalised elastic constants

Next we examine how the elastic constants and critical buckling change with temperature. We plot $\kappa_{\rm R}, Y_{\rm R}$, and $\epsilon_{\rm c}$, obtained from MD simulations, as a function of $W_0/\ell_{\rm th}$ in Fig. 5. At very low temperatures, when $W_0/\ell_{\rm th} \ll 1$ and $L_0/\ell_{\rm p} \ll 1$, these three parameters approach their zero-temperature values. In this regime thermal fluctuations are weak, and thus our system behaves like a classical ribbon. In the $W_0/\ell_{\rm th} > 1$ regime, on the other hand, we see stiffening in $\kappa_{\rm R}$ and softening in $Y_{\rm R}$. We test Eqs. (15) and (16) by fitting our data for $W_0/\ell_{\rm th} > 1$ and $L_0/\ell_{\rm p} < 1$ to the following expressions:

$$\frac{Y_{\rm R}}{Y} = A_Y x^{-\eta_u}, \quad \frac{\kappa_{\rm R}}{\kappa} = A_\kappa x^{\eta}, \quad \frac{\epsilon_{\rm c}}{\epsilon_c^{T=0}} = A_\epsilon x^{\eta+\eta_u}, \quad (20)$$

where $x = W_0/\ell_{\rm th}$.

We first set the exponents to their expected values $\eta=0.8$ and $\eta_u=0.4$ and fit only the A_i to check for consistency. The fits are excellent for the three quantities, with χ^2 goodness-of-fit estimators per degree of freedom of $\chi_Y^2/\text{d.o.f.} = 4.04/6$, $\chi_\kappa^2/\text{d.o.f.} = 3.01/6$ and $\chi_\epsilon^2/\text{d.o.f.} = 5.69/6$.

We have also tried to compute the exponents independently with fits to Eq. (20) without restricting their values. This is a difficult computation [28], since the range of $W_0/\ell_{\rm th}$ that can be accessed in thermalised simulations is limited. We have, however, obtained reasonable estimates

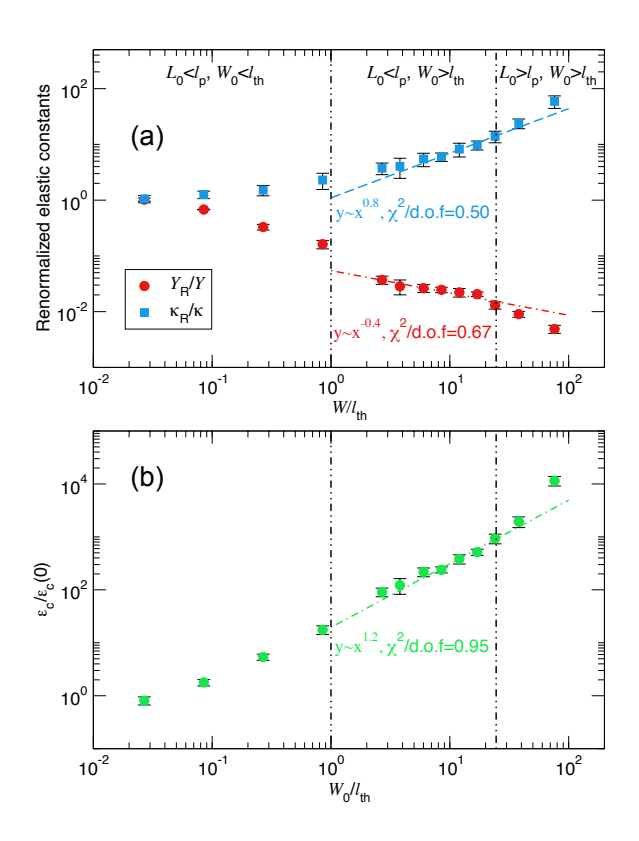


Figure 5: (a) Young's modulus $Y_{\rm R}$, bending rigidity $\kappa_{\rm R}$ and (b) critical strain $\epsilon_{\rm c}$ as a function of $W_0/\ell_{\rm th}$. The expected theoretical scaling of Eq. (20) is an excellent fit in the regime $W_0 > \ell_{\rm th}, L_0 < \ell_{\rm p}$ with $\eta = 0.8$ and $\eta_u = 0.4$.

of $\eta_u=0.41(10)$ and $\eta=0.67(18)$. The Young's modulus $Y_{\rm R}$ softens as the ribbon length L_0 becomes comparable to the persistence length $\ell_{\rm p}$. Very recent work by Morshedifard et al. also found an increase in buckling load of square sheets with increasing temperature [24]. It has also been shown in Ref. [40] that the critical buckling strain of MoS₂ sheets (described by a Stillinger-Weber potential) increases with increasing temperature. To summarise, in the semi-flexible regime where $L_0 < \ell_{\rm p}$ and $\ell_{\rm th} < W$ we find that the mechanics of thin ribbons becomes temperature dependent with $Y_{\rm R} \propto T^{-\eta_u/2}$, $\kappa_{\rm R} \propto T^{\eta/2}$, and $\epsilon_{\rm c} \propto T^{(\eta_u+\eta)/2}$.

5. Conclusions

In this letter we demonstrate that the buckling of thermalized ribbons, when studied via molecular dynamics simulations, can be described by a mean-field theory with renormalized elastic constants when the ribbon length is shorter than the persistence length. We provide three independent ways of locating the buckling transition. In the first approach we use the stress-strain curve to locate buckling and indeed find that the buckling is *delayed* with

increasing temperature. The second approach is via height fluctuations (Appendix B), in analogy with the study of susceptibility in magnetic systems. Such an increase in height fluctuations close to the buckling transition was recently observed in the study of buckling of 1D colloidal systems [41]. Lastly, we find that the height becomes highly sensitive to an out-of-plane symmetry-breaking field \mathcal{E} close to the transition.

While the buckling transitions of thermalised nanoribbons and phase transitions in magnetic systems seem to share similar behaviours, the critical buckling strain is system-size dependent ($\epsilon_{\rm c} \propto 1/L^2$), whereas the critical temperature of a magnetic system is typically independent of system size. Our simulations suggest regions in which the mean-field theory approximately holds. These regions are determined by the ratio between the system sizes (L_0, W_0) and the relevant thermal lengths $(\ell_{\rm th}, \ell_{\rm p})$. In the low temperature regime $(L_0 < \ell_p \text{ and } \ell_{th} > W_0)$, the classical (zero temperature) plate theory holds. In the intermediate (semi-flexible) regime where $L_0 < \ell_{\rm p}$ and $\ell_{\rm th}$ < W_0 we find that the mechanics of thin ribbons with fixed width W_0 can be described with a meanfield theory with temperature dependent elastic constants $Y_{\rm R} \propto T^{-\eta_u/2}, \, \kappa_{\rm R} \propto T^{\eta/2}.$

Because of the softening in Y_R and stiffening in κ_R , the buckling threshold increases with temperature, $\epsilon_{\rm c} \propto$ $T^{(\eta_u+\eta)/2}$. Normally η and η_u are extracted from the Fourier modes of height fluctuations and in-plane phonons. Here, we demonstrate that we can use an Euler buckling to measure these exponents directly. Current nanofabrication techniques can create nanoribbons as thin as ~ 2 nm via transmission electron microscopy [42] and their temperature can be controlled from as low as a few Kelvin up to room temperature [43]. For graphene the thermal length at 300 K is around 3 nm, while for 1 K $\ell_{\rm th} \approx 50$ nm. It should therefore be possible to fabricate ribbons with width to thermal length ratio from roughly 0.01 to 100. A similar setup including an out-of-plane symmetry-breaking field has been achieved experimentally [44]. The simulations and theory presented here provide predictions for buckling of thermalised nanoribbons that can be tested experimentally. The tunability of buckling via compression, temperature, and perturbing field could be the useful for development of mechanics-based non-volatile memories.

Declaration of competing interests

The authors declare that they have no known competing financial interests or personal relationships that could have appeared to influence the work reported in this paper.

Acknowledgements

This research was supported in part by the National Science Foundation under grant no. NSF-PHY-1748958. Work by PZH and DRN was also supported through the

NSF grant DMR-1608501 and via the Harvard Materials Science Research and Engineering Center, through NSF grant DMR-2011754. The work of MJB was also partially supported by the NSF through the Materials Science and Engineering Center at UC Santa Barbara, DMR-1720256 (iSuperSeed). DY was supported by the Chan Zuckerberg Biohub and received funding from the Ministerio de Economía, Industria y Competitividad (MINECO, Spain); the Agencia Estatal de Investigación (AEI, Spain) and Fondo Europeo de Desarrollo Regional (FEDER, EU) through grant no. PGC2018-094684-B-C21. DY and SB thank the KITP for hospitality during part of this project. PZH and DRN thank Abigail Plummer and Suraj Shankar for helpful discussions. MB and DRN acknowledge helpful conversations with Daniel Lopez. The computations in this paper were run on the FASRC Cannon cluster supported by the FAS Division of Science Research Computing Group at Harvard University. Some simulations were carried out on the Syracuse University HTC Campus Grid, which is supported by NSF-ACI-1341006.

Appendix A. Numerical check of the T = 0 theory

To check that our coarse-grained model is consistent with the zero-temperature theory we simulated systems with $L_0=100a, W_0=20a, \hat{\kappa}=2.5, k/\hat{\kappa}=1440/a^2$ at T=0. The energy is minimised using the FIRE algorithm. Recall that the connection between continuum elastic constants and those for a triangular lattice is $\kappa=\frac{\sqrt{3}\hat{\kappa}}{2}$ and $Y=\frac{2k}{\sqrt{3}}$. We plot the height amplitude $h_{\rm M}$ and stress σ as a function of the compressive strain ($\epsilon=1-L_{\epsilon}/L_0$) in Fig. A.6. Our simulations produce a square-root scaling of the buckling amplitude, in agreement with the mean field theory. The computed Young's modulus, critical stress, and critical strain are within 10% of the theoretical predictions [$\frac{Y_{\rm simulation}}{Y_{\rm theory}}=0.99, \frac{\sigma_{\rm c}^{\rm simulation}}{\sigma_{\rm c}^{\rm theory}}=0.92, \frac{\sigma_{\rm c}^{\rm simulation}}{\sigma_{\rm c}^{\rm theory}}=0.94$]. We attribute the small deviations to our discretised clamped boundary conditions.

Appendix B. Stress-strain curve

We fit data points close to $\epsilon=0$ to obtain $Y_{\rm R}$ and fit data points beyond the buckling point to obtain the linear asymptotic behaviour. We use the intersection of these two lines to estimate the critical buckling load $\sigma_{\rm c}$ and critical buckling strain $\epsilon_{\rm c}$. By plotting the scaled stress $\sigma/\sigma_{\rm c}^{\rm theory}$ as a function of ϵ , we can see that scaled critical buckling load $\sigma_{\rm c}/\sigma_{\rm c}^{\rm theory}$ increases with increasing $W_0/\ell_{\rm th}$ (increasing T), whereas the slope $(Y_{\rm R})$ decreases with increasing $W_0/\ell_{\rm th}$, in accordance with the theoretical expectation (see Fig. B.7).

Appendix B.1. The temperature-dependent critical strain from height susceptibility

Since we are interested in the buckling response due to external field we study the height susceptibility defined as

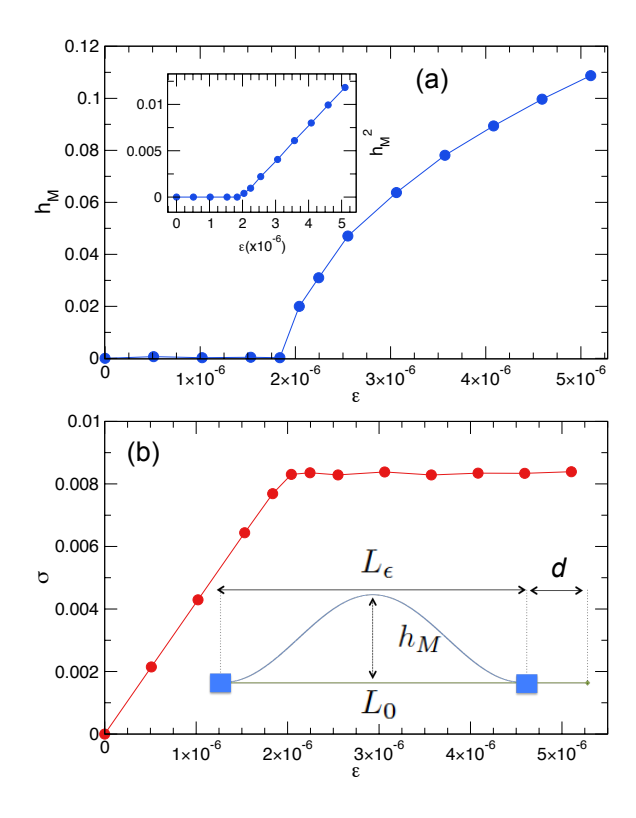


Figure A.6: The maximum height $h_{\rm M}$ (a) and the longitudinal stress σ (b) at T=0 as a function of the compressive strain $\epsilon=1-L_\epsilon/L_0$. The inset in (a) shows the linear relationship between $h_{\rm M}^2$ and ϵ for $\epsilon>\epsilon_{\rm C}$.

 $\chi = d\langle h_{CM} \rangle / d\mathcal{E}$. We can directly obtain χ using height fluctuations with Eq. (9).

As discussed in the main text, the height of center of mass $h_{\rm CM}$ beyond buckling obtained from simulations of finite systems might flip after a long finite time. Thus $h_{\rm CM}$ of independent runs average to zero. In simulations of classical Ising spins it is common to take the absolute value of the order parameter [45], a strategy that can be adopted to our problem:

$$\chi[|h_{\rm CM}|] \propto \langle h_{\rm CM}^2 \rangle - \langle |h_{\rm CM}| \rangle^2.$$
 (B.1)

Note that this quantity differs from the true susceptibility (see eq 9). In MD simulations we can apply a small symmetry-breaking field to bias the system to buckle in one direction. Specifically, we simulated a system with $W_0/\ell_{\rm th} \sim 8.5$ and compare these two quantities. The function $\chi[|h_{\rm CM}|]$ has a similar qualitative behavior and similar peak location to $\chi[h_{\rm CM}]$, as shown in fig. B.8. To save computing time we use $\chi[|h_{\rm CM}|]$ of eq. (B.1) to locate the peaks. The susceptibilities $(\chi[|h_{\rm CM}|])$ for several temperatures as a function of the compressive strain ϵ are plotted in fig. B.9. Here and in following plots we indicate the temperature through the ratio of the system's width to

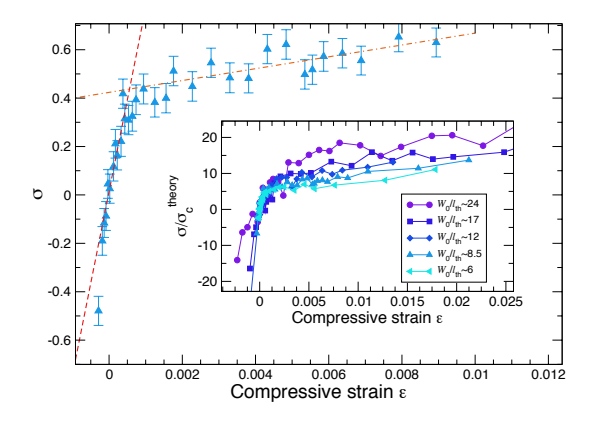


Figure B.7: Average stress σ as a function of compressive strain ϵ for a ribbon with at a temperature large enough so that $W_0/\ell_{\rm th}=8.5$. The dashed lines are linear fits in the pre-buckling (small- ϵ) regime and in the post-buckling regime $\epsilon > \epsilon_{\rm c}$. The inset shows the scaled stress $\sigma/\sigma_{\rm c}^{\rm theory}$ for different systems. The scaled critical buckling, which is proportional to the renormalised bending rigidity $\kappa_{\rm R}$, increases with increasing $W_0/\ell_{\rm th}$ (or temperature). In contrast, the slope $(Y_{\rm R})$ becomes smaller with increasing $W_0/\ell_{\rm th}$.

its thermal length, which is the appropriate scaling variable. We can clearly see that the buckling transition persists for finite T, while the position of the peaks increases with increasing $W_0/\ell_{\rm th}$. This trend is consistent with our theoretical prediction that $\epsilon_{\rm c}$ should increase as the renormalisation of the Young's modulus and bending rigidity becomes more and more important. We find a proportionality between the critical strains obtained from stress-strain curves and critical strains obtained from the peaks of χ ; however, these critical strain obtained from two different approaches do not coincide exactly (see Fig. B.10).

Appendix C. Variational approach

Here we describe how eliminating in-plane displacement fields leads to a non-local stretching term in the Gibbs energy. For a clamped 1D ribbon we write the effective 1D Young's modulus as $Y_{1D} = YW_0$ and the bending rigidity as $\kappa_{1D} = \kappa W_0$. The amount of work is -Fd and the compression distance d can be approximated as follows.

$$L_{\epsilon} + d \simeq \int_{-L_{\epsilon}/2}^{L_{\epsilon}/2} \sqrt{1 + \left(\frac{\mathrm{d}h}{\mathrm{d}x}\right)^2} \mathrm{d}x$$
 (C.1)

$$d \simeq \frac{1}{2} \int_{-L_{\star}/2}^{L_{\epsilon}/2} \left(\frac{\mathrm{d}h}{\mathrm{d}x}\right)^2 \mathrm{d}x. \tag{C.2}$$

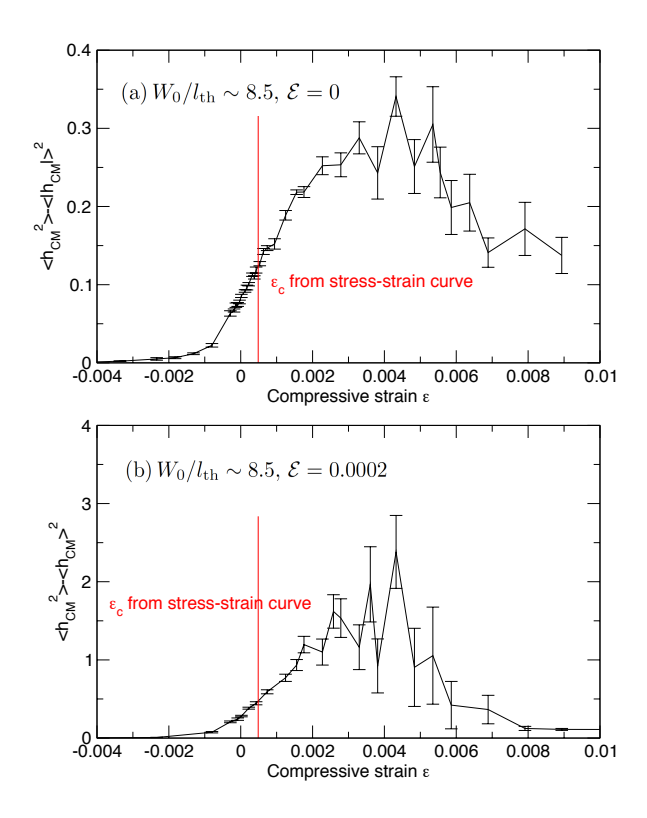


Figure B.8: (a) The susceptibility of the absolute value centre-of-mass height $\chi[|h_{\rm CM}|]$ as a function of the compressive strain ϵ with $\mathcal{E}=0$ and (b) the susceptibility of centre-of-mass height $\chi[h_{\rm CM}]$ as a function of the compressive strain ϵ with symmetry-breaking field $\mathcal{E}=0.0002$ for a system with $W_0/\ell_{\rm th}\sim 8.5$. The locations of the peaks are similar, and occur beyond the buckling strain $\epsilon_{\rm c}$.

We assume variations only in the x-direction. The Gibbs free energy is given by

$$\begin{split} G[u_x,h] = & \frac{\kappa_{\text{1D}}}{2} \int_{-L_{\epsilon}/2}^{L_{\epsilon}/2} \mathrm{d}x \left(\frac{\mathrm{d}^2 h}{\mathrm{d}x^2}\right)^2 \\ & + \frac{Y_{\text{1D}}}{2} \int_{-L_{\epsilon}/2}^{L_{\epsilon}/2} \mathrm{d}x \left[\frac{\mathrm{d}u}{\mathrm{d}x} + \frac{1}{2} \left(\frac{\mathrm{d}h}{\mathrm{d}x}\right)^2\right]^2 \\ & - \frac{F}{2} \int_{-L_{\epsilon}/2}^{L_{\epsilon}/2} \mathrm{d}x \left(\frac{\mathrm{d}h}{\mathrm{d}x}\right)^2, \end{split} \tag{C.3}$$

where $F=W_0\sigma_{xx}$. We will now focus on the middle stretching term $G_{\rm s}$ controlled by $Y_{\rm 1D}$. As is typically done in the 2D case, we focus on the vector-potential-like contribution, $A(x)=\frac{1}{2}\left(\frac{{\rm d}h}{{\rm d}x}\right)^2$, and we write the fields in Fourier

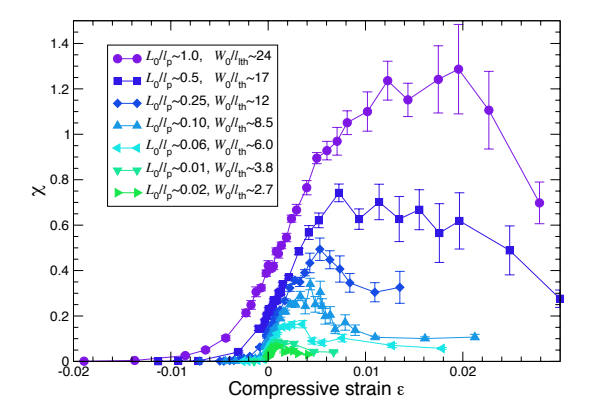


Figure B.9: The susceptibility of the absolute centre-of-mass height $\chi[|h_{\rm CM}|]$ as a function of the compressive strain ϵ . The position of the peak increases with the thermal length $\ell_{\rm th}$. This is in accordance with the theoretical expectation of a delayed buckling transition with increasing T, due to thermal stiffening. The simulated systems cover the temperature range of $0.005 \leq k_{\rm B}T/\hat{\kappa} \leq 0.4$.

space as,

$$\frac{\mathrm{d}u}{\mathrm{d}x} = U_0 + \sum_{q \neq 0} \mathrm{i}q\tilde{u}(q)\mathrm{e}^{\mathrm{i}qx} \tag{C.4}$$

$$A = A_0 + \sum_{q \neq 0} \tilde{A}(q)e^{iqx}, \qquad (C.5)$$

where we have separated out the q=0 modes. The stretching energy $G_{\rm s}$ is given by

$$G_{s} = \frac{Y_{1D}}{2} \int_{-L_{\epsilon}/2}^{L_{\epsilon}/2} dx \left[U_{0} + A_{0} + \sum_{q \neq 0} \left(iq\tilde{u}(q) + \tilde{A}(q) \right) e^{iqx} \right]$$

$$\times \left[U_{0} + A_{0} + \sum_{q \neq 0} \left(iq'\tilde{u}(q') + \tilde{A}(q') \right) e^{iq'x} \right]$$

$$= \frac{Y_{1D}}{2} L_{\epsilon} (U_{0} + A_{0})^{2}$$

$$+ \frac{Y_{1D}}{2} \sum_{q \neq 0} \sum_{q' \neq 0} \int_{-L_{\epsilon}/2}^{L_{\epsilon}/2} e^{i(q+q')x} \left(iq\tilde{u}(q) + \tilde{A}(q) \right)$$

$$\times \left(iq'\tilde{u}(q') + \tilde{A}(q') \right) dx$$

$$= \frac{Y_{1D}}{2} L_{\epsilon} (U_{0} + A_{0})^{2} + \frac{Y_{1D}L_{\epsilon}}{2} \sum_{q \neq 0} |iq\tilde{u}(q) + \tilde{A}(q)|^{2}.$$
(C.6)

The stretching energy G_s is clearly minimised when $\tilde{u}(q) = -i\tilde{A}(q)/q$. Upon imposing constant strain and the bound-

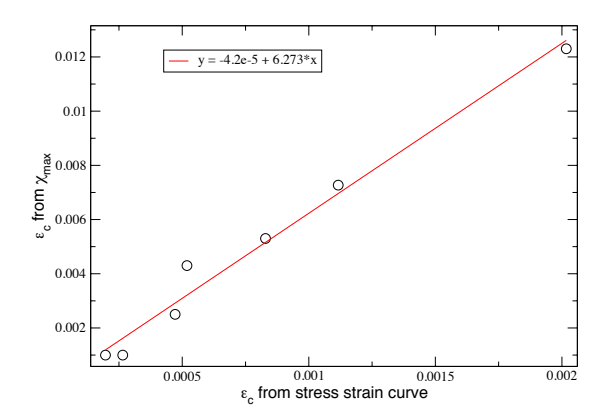


Figure B.10: Critical strains obtained from the peaks of χ (eq. (B.1)) as a function of critical strains obtained from stress-strain curves.

ary conditions we find,

$$U_0 = \frac{1}{L_{\epsilon}} \int_{-L_{\epsilon}/2}^{L_{\epsilon}/2} dx \, \frac{du}{dx} = \frac{1}{L_{\epsilon}} [u(L_{\epsilon}/2) - u(-L_{\epsilon}/2)] = 0,$$
(C.7)

and similarly,

$$A_0 = \frac{1}{L_{\epsilon}} \int_{-L_{\epsilon}/2}^{L_{\epsilon}/2} dx \ A = \frac{1}{L_{\epsilon}} \int_{-L_{\epsilon}/2}^{L_{\epsilon}/2} \frac{1}{2} \left(\frac{dh}{dx}\right)^2 dx. \quad (C.8)$$

Upon substituting Eq. (C.6) in the form $G_s = \frac{Y_{1D}}{2} L_{\epsilon} A_0^2$ into Eq C.3, we obtain the free energy of Eq (10) of the main text, provided we include a contribution from the symmetry-breaking field.

We now discuss an out-of-plane field that couples to the height. For instance, if we put uniform charges on the ribbon and place it within a uniform electric field, the potential energy is $V_{\perp} = -\int_{-L_{\epsilon}/2}^{L_{\epsilon}/2} \rho \mathcal{E} \, h \, \mathrm{d}x$. After collecting terms, including an out-of-plane external electric field \mathcal{E} , we obtain the Gibbs energy

$$G[h, \mathcal{E}] = \frac{\kappa_{1D}}{2} \int_{-L_{\epsilon}/2}^{L_{\epsilon}/2} dx \left(\frac{d^{2}h}{dx^{2}}\right)^{2}$$

$$+ \frac{Y_{1D}}{2L_{\epsilon}} \left[\int_{-L_{\epsilon}/2}^{L_{\epsilon}/2} dx \frac{1}{2} \left(\frac{dh}{dx}\right)^{2} \right]^{2}$$

$$- \frac{F}{2} \int_{-L_{\epsilon}/2}^{L_{\epsilon}/2} dx \left(\frac{dh}{dx}\right)^{2} - \rho \mathcal{E} \int_{-L_{\epsilon}/2}^{L_{\epsilon}/2} h dx.$$
(C.9)

Close to the buckling transition we focus on the first buckling mode $h = h_{\rm M} \frac{1}{2} \left[1 + \cos \left(\frac{2\pi x}{L_{\epsilon}} \right) \right]$, where h_M is the

height amplitude, as an ansatz that insures tangential boundary conditions $\frac{\mathrm{d}h(x)}{\mathrm{d}x}\Big|_{x\pm=L_{\epsilon}/2}=0$. We then obtain Eq. (11) of the main text,

$$G = \frac{\pi^2}{4L_{\epsilon}} \left(\frac{4\kappa_{1D}\pi^2}{L_{\epsilon}^2} - F \right) h_{\rm M}^2 + \frac{\pi^4 Y_{1D}}{32L_{\epsilon}^3} h_{\rm M}^4 - \frac{\rho L_{\epsilon}\mathcal{E}}{2} h_{\rm M}.$$
(C.10)

It is helpful to write the above equation in terms of new parameters $a,b,\epsilon_{\rm c}$

$$G = a(\epsilon - \epsilon_{\rm c})h_{\rm M}^2 + bh_{\rm M}^4 - \frac{\rho L_{\epsilon} \mathcal{E}}{2}h_{\rm M}, \qquad (C.11)$$

where $a=\frac{Y_{\rm 1D}\pi^2}{4L_\epsilon},\ b=\frac{\pi^4Y_{\rm 1D}}{32L_\epsilon^3},\ \epsilon_{\rm c}=\frac{4\pi^2\kappa_{\rm 1D}}{Y_{\rm 1D}L_\epsilon^2}.$ Upon minimising the Gibbs free energy by setting $\frac{{\rm d}G}{{\rm d}h_M}\Big|_{\mathcal{E}=0}=0$, we find

$$h_{M} = \begin{cases} 0, & \text{if } \epsilon < \epsilon_{\text{c}} \\ \pm \sqrt{\frac{a}{2b}(\epsilon - \epsilon_{\text{c}})} = \frac{2L_{\epsilon_{\text{c}}}}{\pi} \sqrt{\epsilon - \frac{4\kappa\pi^{2}}{YL_{\epsilon_{\text{c}}}^{2}}}, & \text{if } \epsilon > \epsilon_{\text{c}} \end{cases}$$

(C.12)

Appendix C.1. Susceptibility

To obtain the susceptibility at zero external field we first solve $\frac{dG}{dh_M}=0$, which leads to

$$0 = 2ah_M(\epsilon_c - \epsilon) + 4bh_M^3 - \frac{\rho L_{\epsilon} \mathcal{E}}{2}$$
 (C.13)

$$\mathcal{E} = \frac{2}{\rho L_{\epsilon}} [4bh_{\mathrm{M}}^{3} + 2a(\epsilon_{\mathrm{c}} - \epsilon)h_{\mathrm{M}}]. \tag{C.14}$$

We can now calculate the susceptibility and use $\rho = Q/L_0$ and $Y_{1D} = YW_0$ to obtain

$$\frac{\partial h_{\rm M}}{\partial \mathcal{E}} \bigg|_{\mathcal{E}=0} = \begin{cases} \frac{Q}{Y\pi^2} \frac{L_{\epsilon_{\rm c}}}{W_0} (\epsilon_{\rm c} - \epsilon)^{-1} & \text{if } \epsilon < \epsilon_{\rm c} \\ \frac{Q}{2Y\pi^2} \frac{L_{\epsilon_{\rm c}}}{W_0} (\epsilon - \epsilon_{\rm c})^{-1} & \text{if } \epsilon > \epsilon_{\rm c} \end{cases}$$
(C.15)

For a ribbon in a gravitational field simply replace $\mathcal{E} = g$ and Q = m, where m is the total mass.

References

- B. Grosso, E. Mele, Graphene gets bent, Physics Today 73 (2020) 46. doi:10.1063/PT.3.4569.
- [2] M. K. Blees, A. W. Barnard, P. A. Rose, S. P. Roberts, K. L. McGill, P. Y. Huang, A. R. Ruyack, J. W. Kevek, B. Kobrin, D. A. Muller, P. L. McEuen, Graphene kirigami, Nature 524 (2015) 204–207. doi:10.1038/nature14588.
- [3] T. C. Shyu, P. F. Damasceno, P. M. Dodd, A. Lamoureux, L. Xu, M. Shlian, M. Shtein, S. C. Glotzer, N. A. Kotov, A kirigami approach to engineering elasticity in nanocomposites through patterned defects, Nature materials 14 (8) (2015) 785. doi:10.1038/nmat4327.
- [4] P. Z. Hanakata, Z. Qi, D. K. Campbell, H. S. Park, Highly stretchable MoS₂ kirigami, Nanoscale 8 (1) (2016) 458–463. doi:10.1039/C5NR06431G.

- [5] Y. Tang, J. Yin, Design of cut unit geometry in hierarchical kirigami-based auxetic metamaterials for high stretchability and compressibility, Extreme Mechanics Letters 12 (2017) 77-85. doi:10.1016/j.eml.2016.07.005.
- [6] A. Rafsanjani, K. Bertoldi, Buckling-induced kirigami, Phys. Rev. Lett. 118 (2017) 084301. doi:10.1103/PhysRevLett.118. 084301.
- [7] P. Z. Hanakata, E. D. Cubuk, D. K. Campbell, H. S. Park, Accelerated search and design of stretchable graphene kirigami using machine learning, Physical review letters 121 (25) (2018) 255304. doi:10.1103/PhysRevLett.121.255304.
- [8] M. Moshe, E. Esposito, S. Shankar, B. Bircan, I. Cohen, D. R. Nelson, M. J. Bowick, Kirigami mechanics as stress relief by elastic charges, Phys. Rev. Lett. 122 (2019) 048001. doi:10.1103/PhysRevLett.122.048001.
- [9] Y. Yang, M. A. Dias, D. P. Holmes, Multistable kirigami for tunable architected materials, Physical Review Materials 2 (11) (2018) 110601. doi:10.1103/PhysRevMaterials.2.110601.
- [10] M. A. Dias, M. P. McCarron, D. Rayneau-Kirkhope, P. Z. Hanakata, D. K. Campbell, H. S. Park, D. P. Holmes, Kirigami actuators, Soft matter 13 (48) (2017) 9087–9092. doi:10.1039/ C7SM01693.I.
- [11] A. Rafsanjani, Y. Zhang, B. Liu, S. M. Rubinstein, K. Bertoldi, Kirigami skins make a simple soft actuator crawl, Science Robotics 3 (2018) eaar7555. doi:10.1126/scirobotics. aar7555.
- [12] Y. Morikawa, S. Yamagiwa, H. Sawahata, R. Numano, K. Koida, T. Kawano, Donut-shaped stretchable kirigami: Enabling electronics to integrate with the deformable muscle, Advanced Healthcare Materials 8 (23) (2019) 1900939. doi: 10.1002/adhm.201900939.
- [13] M. Katsnelson, Graphene: carbon in two dimensions, Cambridge University Press, 2012.
- [14] D. Nelson, T. Piran, S. Weinberg, Statistical Mechanics of Membranes and Surfaces, 2nd Edition, World Scientific, Singapore, 2004.
- [15] D. Nelson, L. Peliti, Fluctuations in membranes with crystalline and hexatic order, J. Phys. France 48 (1987) 1085–1092. doi: 10.1051/jphys:019870048070108500.
- [16] J. A. Aronovitz, T. C. Lubensky, Fluctuations of solid membranes, Phys. Rev. Lett. 60 (1988) 2634–2637. doi:10.1103/PhysRevLett.60.2634.
- [17] E. Guitter, F. David, S. Leibler, L. Peliti, Thermodynamical behavior of polymerized membranes, Journal de Physique 50(14) (1989) 1787–1819. doi:10.1051/jphys:0198900500140178700.
- [18] P. Le Doussal, L. Radzihovsky, Self-consistent theory of polymerized membranes, Phys. Rev. Lett. 69 (1992) 1209–1212. doi:10.1103/PhysRevLett.69.1209.
- [19] Z. Zhang, H. T. Davis, D. M. Kroll, Scaling behavior of self-avoiding tethered vesicles, Phys. Rev. E 48 (1993) R651–R654. doi:10.1103/PhysRevE.48.R651.
- [20] M. J. Bowick, S. M. Catterall, M. Falcioni, G. Thorleifsson, K. N. Anagnostopoulos, The flat phase of crystalline membranes, J. Phys. I France 6 (1996) 1321–1345. doi:10.1051/jp1: 1996139.
- [21] A. Košmrlj, D. R. Nelson, Mechanical properties of warped membranes, Physical Review E 88 (1) (2013) 012136.
- [22] K. N. Kudin, G. E. Scuseria, B. I. Yakobson, C₂F, BN, and C nanoshell elasticity from ab initio computations, Physical Review B 64 (23) (2001) 235406. doi:10.1103/PhysRevB.64. 235406.
- [23] A. Košmrlj, D. R. Nelson, Response of thermalized ribbons to pulling and bending, Phys. Rev. B 93 (2016) 125431. doi: 10.1103/PhysRevB.93.125431.
- [24] A. Morshedifard, M. Ruiz-Garcia, M. J. A. Qomi, A. Kosmrlj, Buckling of thermalized elastic sheets, arXiv preprintarXiv: 2005.05949.
- [25] A. Stukowski, Visualization and analysis of atomistic simulation data with OVITO-the open visualization tool, Modelling and Simulation in Materials Science and Engineering 18. doi:10. 1088/0965-0393/18/1/015012.

- [26] M. J. Bowick, A. Travesset, The statistical mechanics of membranes, Phys. Rep. 344 (2001) 255–308. doi:10.1016/ S0370-1573(00)00128-9.
- [27] H. S. Seung, D. R. Nelson, Defects in flexible membranes with crystalline order, Phys. Rev. A 38 (1988) 1005-1018. doi:10. 1103/PhysRevA.38.1005.
- [28] M. J. Bowick, A. Košmrlj, D. R. Nelson, R. Sknepnek, Non-Hookean statistical mechanics of clamped graphene ribbons, Physical Review B 95 (10) (2017) 104109. doi:10.1103/ PhysRevB.95.104109.
- [29] D. Yllanes, S. S. Bhabesh, D. R. Nelson, M. J. Bowick, Thermal crumpling of perforated two-dimensional sheets, Nat. Comm. 8 (2017) 1381. doi:10.1038/s41467-017-01551-y.
- [30] D. Yllanes, D. R. Nelson, M. J. Bowick, Folding pathways to crumpling in thermalized elastic frames, Phys. Rev. E 100 (2019) 042112. doi:10.1103/PhysRevE.100.042112.
- [31] J. A. Anderson, J. Glaser, S. C. Glotzer, HOOMD-blue: A Python package for high-performance molecular dynamics and hard particle monte carlo simulations, Computational Materials Science 173 (2020) 109363. doi:10.1016/j.commatsci.2019. 109363.
- [32] A. P. Young, Everything you wanted to know about Data Analysis and Fitting but were afraid to ask, Springer, Berlin, 2015. arXiv:1210.3781.
- [33] L. D. Landau, E. M. Lifshitz, Theory of Elasticity, 3rd Edition, Butterworth-Heinemann,, Singapore, 1999.
- [34] R. Lifshitz, M. Cross, Nonlinear dynamics of nanomechanical and micromechanical resonators, Reviews of nonlinear dynamics and complexity 1 (2008) 1–52. doi:10.1002/9783527626359.
- [35] J.-P. Kownacki, D. Mouhanna, Crumpling transition and flat phase of polymerized phantom membranes, Phys. Rev. E 79 (2009) 040101. doi:10.1103/PhysRevE.79.040101.
- [36] J. Los, M. I. Katsnelson, O. Yazyev, K. Zakharchenko, A. Fasolino, Scaling properties of flexible membranes from atomistic simulations: application to graphene, Physical Review B 80 (12) (2009) 121405. doi:10.1103/PhysRevB.80.121405.
- [37] R. Roldán, A. Fasolino, K. V. Zakharchenko, M. I. Katsnelson, Suppression of anharmonicities in crystalline membranes by external strain, Physical Review B 83 (17) (2011) 174104. doi:10.1103/PhysRevB.83.174104.
- [38] J. Zinn-Justin, Quantum Field Theory and Critical Phenomena, 4th Edition, Clarendon Press, Oxford, 2005.
- [39] S. S. Bhabesh, P. Z. Hanakata, M. J. Bowick, D. R. Nelson, D. Yllanes, to be published.
- [40] J. W. Jiang, The buckling of single-layer MoS_2 under uniaxial compression, Nanotechnology 25 (35) (2014) 355402. doi:10. 1088/0957-4484/25/35/355402.
- [41] S. Stuij, J. M. van Doorn, T. Kodger, J. Sprakel, C. Coulais, P. Schall, Stochastic buckling of self-assembled colloidal structures, Physical Review Research 1 (2019) 023033. doi:10.1103/ PhysRevResearch.1.023033.
- [42] P. Masih Das, G. Danda, A. Cupo, W. M. Parkin, L. Liang, N. Kharche, X. Ling, S. Huang, M. S. Dresselhaus, V. Meunier, et al., Controlled sculpture of black phosphorus nanoribbons, ACS nano 10 (2016) 5687–5695. doi:10.1021/acsnano. 6b02435.
- [43] I. R. Storch, R. De Alba, V. P. Adiga, T. Abhilash, R. A. Barton, H. G. Craighead, J. M. Parpia, P. L. McEuen, Young's modulus and thermal expansion of tensioned graphene membranes, Physical Review B 98 (8) (2018) 085408. doi:10.1103/PhysRevB.98.085408.
- [44] N. Lindahl, D. Midtvedt, J. Svensson, O. A. Nerushev, N. Lindvall, A. Isacsson, E. E. Campbell, Determination of the bending rigidity of graphene via electrostatic actuation of buckled membranes, Nano letters 12 (2012) 3526–3531. doi:10.1021/nl301080v.
- [45] A. W. Sandvik, Computational studies of quantum spin systems, in: AIP Conference Proceedings, Vol. 1297, American Institute of Physics, 2010, pp. 135–338.